Alkali desorption from ilmenite oxygen carrier particles used in biomass combustion

Fuel 359 (2024) 130400

Contents lists available at ScienceDirect

Fuel

journal homepage: www.elsevier.com/locate/fuel

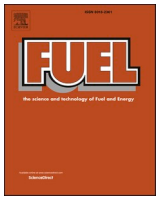

Full Length Article

Alkali desorption from ilmenite oxygen carrier particles used in biomass combustion

Viktor Andersson [a], Ivana Staničić [b], Xiangrui Kong [a], Henrik Leion [c], Tobias Mattisson [b], Jan B.C. Pettersson [a,*]

[a] Department of Chemistry and Molecular Biology, Atmospheric Science, University of Gothenburg, Medicinaregatan 7B, SE-413 90 Gothenburg, Sweden
[b] Department of Space, Earth and Environment, Division of Energy Technology, Chalmers University of Technology, Hörsalsvägen 7A, SE-412 96 Gothenburg, Sweden
[c] Energy and Materials, Chemistry and Chemical Engineering, Chalmers University of Technology, Kemigården 4, SE-412 96 Gothenburg, Sweden

ARTICLE INFO

Keywords:
Ilmenite
Alkali
Surface ionization
Kinetics
Oxygen carrier
Biomass conversion

ABSTRACT

Oxygen-carrying fluidized bed materials are increasingly used in novel technologies for carbon capture and storage, and to improve the efficiency of fuel conversion processes. Potassium- and sodium-containing compounds are released during biomass combustion and may have both negative and positive effects on conversion processes. Ilmenite is an important oxygen carrier material with the ability to capture alkali in the form of titanates. This is a desirable property since it may reduce detrimental alkali effects including fouling, corrosion, and fluidized bed agglomeration. This study investigates the interactions of alkali-containing compounds with ilmenite particles previously used in an industrial scale (115 MW_{th}) oxygen carrier aided combustion system. The ilmenite samples were exposed to temperatures up to 1000 °C under inert and oxidizing conditions while the alkali release kinetics were characterized using online alkali monitoring. Alkali desorption occurs between 630 and 800 °C, which is attributed to loosely bound alkali at or near the surface of the particles. Extensive alkali release is observed above 900 °C and proceeds during extended time periods at 1000 °C. The release above 900 °C is more pronounced under oxidizing conditions and approximately 9.1 and 3.2 wt% of the alkali content is emitted from the ilmenite samples in high and low oxygen activity, respectively. Detailed material analyses using scanning electron microscopy with energy dispersive X-ray spectroscopy and X-ray photoelectron spectroscopy were conducted before and after temperature treatment, which revealed that the concentrations of potassium, sodium and chlorine decrease at the outermost surface of the ilmenite particles during temperature treatment, and Cl is depleted to a deeper level in oxidizing conditions compared to inert. The implications for ilmenite-ash interactions, oxygen carrier aided combustion and chemical looping systems are discussed.

1. Introduction

Global warming caused by anthropogenic emissions of CO_2 is one of the largest challenges in modern times [1]. The Paris agreement states that decarbonization of the world energy systems should be reached within a few decades, and the global temperature increase should be limited to below 2 °C, and preferably below 1.5 °C, above the pre-industrial level [2]. Replacing fossil fuels with biofuels that may be considered to be renewable and CO_2-neutral is one important step towards reaching these goals. If biomass is converted in combustion systems equipped with carbon capture and storage techniques it may be possible to reach negative CO_2 emissions [3–5]. Chemical looping combustion (CLC) is a technology that can reach negative CO_2 emissions when it is combined with bioenergy carbon capture and storage (BECCS) [6]. The process is based on two interconnected circulating fluidized bed (CFB) units that operate with a bed consisting of oxygen carrier (OC) particles [7,8]. The CLC process is characterized by separating the fuel from the combustion air and thus the energy-demanding step of removing nitrogen from the flue gases can be avoided to achieve a highly concentrated stream of CO_2.

The concept of using oxygen carriers in fluidized bed units is not limited to CLC. It is also used in other applications like chemical looping gasification (CLG) [9,10] and oxygen carrier aided combustion (OCAC) [11,12]. The main difference between CLC and OCAC is that the latter only has one fluidized bed combustion chamber and the OC undergoes redox reactions inside this reactor exclusively. The OC is oxidized and

* Corresponding author.
E-mail address: janp@chem.gu.se (J.B.C. Pettersson).

https://doi.org/10.1016/j.fuel.2023.130400
Received 20 June 2023; Received in revised form 13 November 2023; Accepted 13 November 2023
Available online 21 November 2023

reduced when in contact with air and fuel, respectively, and thereby evens out oxygen-rich and oxygen-poor zones that usually are a problem in conventional fluidized bed combustion [13,14]. Hence, the addition of oxygen carriers improves contact between fuel and oxidizing agent and thereby also the combustion efficiency. This enables the use of heterogeneous biomass fuels that can otherwise be problematic to implement due to their varying amounts of volatiles, ash forming elements and water content [15].

One aspect that these conversion systems have in common is the need for a well-functioning OC. The OC needs to have sufficient reactivity, oxygen-carrying ability and attrition strength for the selected process. The optimal OC should also be economically viable and environmentally sound. There are a vast amount of studies focusing on oxygen carriers used for chemical looping or OCAC purposes [8]. There are studies on synthetic (*i.e.* manufactured) materials consisting of monometallic or combined oxides [16,17], which typically reach very high fuel conversion with the drawback of being expensive [18]. In recent years inexpensive oxygen carriers composed of natural ores have also received increased attention. Manganese [19,20] and iron ores [21] are two common materials, but probably one of the most scrutinized ones is ilmenite ore [22,23]. Ilmenite consists mainly of iron and titanium and can be found as natural sand or mined from rock ore, where the latter usually contains more iron. Although some Fe-Ti phases can be oxidized and reduced, the most significant oxygen transferring component in ilmenite is iron, as it alters between Fe^{2+} and Fe^{3+} during reduction and oxidation, forming the oxides FeO and Fe_2O_3. It has been concluded that freshly mined ilmenite needs to be activated before it can transfer sufficient amounts of oxygen [22]. The activation process is carried out with consecutive redox cycles with iron migrating through the lattice structure creating an iron-rich surface during the oxidation and reduction of the material. Therefore, the iron oxide concentration and thus the oxygen-carrying capacity of ilmenite increases with the number of redox cycles [22]. Although the oxygen transfer should increase with time, the complex environment in boilers operated with biomass might reduce the effectiveness of the ilmenite. Not only does biomass have a higher water content and lower heating value compared to fossil fuels, it also contains large amounts of ash components that can interact with the OC [15,24]. Some of the main ash constituents are Ca, K and Na [24]. It has been reported that Ca forms ash layers on the surface of ilmenite particles, which may influence the iron on the surface and thereby the oxygen-carrying ability [25].

Although alkali may have catalytic effects on biochar gasification with increased conversion in comparison to fossil fuels [9,26–28], it is mostly known to harm the process equipment. Alkali chlorides and hydroxides are widely known to cause fouling and corrosion of heat exchanger surfaces as the volatile alkali components condense on the cold surfaces or nucleate to form aerosol particles that impact and deposit on available surfaces [15,29–31]. Therefore, it is potentially an advantage if ilmenite can work as an alkali scavenger by efficiently absorbing potassium [25,32]. Both K and Ca have been seen to diffuse into the particles, forming the titanates $KTi_8O_{16.5}$ and $CaTiO_3$ [11]. Absorption of K does not seem to cause agglomeration of the ilmenite bed material [11,25], which is otherwise an issue when sand or other Si-containing bed materials are used [33–35]. Studies have shown that addition of KCl, K_2CO_3 or K_2SO_4 enhancse the reactivity of ilmenite, while alkali compounds like KPO_3 have a negative effect on reactivity [36]. In addition, ilmenite exposed to potassium has been observed to have a reduced oxygen carrying capacity [37]. Most studies that have investigated the interaction between oxygen carriers and alkali have focused on potassium [11,25,34,36,38], but the knowledge regarding the interaction of sodium with oxygen carriers is scarce. In this study, both K and Na interactions with ilmenite will be addressed and discussed.

There have been studies investigating the build-up of ash layers and migration mechanisms during OCAC [22], but to our knowledge alkali release from ilmenite has not previously been investigated. In a study by Gogolev et al. alkali concentrations were measured in the flue gases leaving both air and fuel reactors in a 100 kW CLC pilot plant during biomass conversion [29]. A mixture of ilmenite and calcium manganite was used as OC. Relatively high alkali concentrations were measured in flue gases leaving the air reactor, which implies that alkali is being transported from the fuel reactor to the air reactor. A possible transportation path can be that the alkali was absorbed by the OC in the fuel reactor and released as the OC entered the air reactor, which is normally at a higher temperature than the fuel reactor. Since most of the heat extraction occurs in proximity to the air reactor, it is important to establish an understanding of possible desorption mechanisms in order to reduce fouling and corrosion of heat exchanger surfaces. Additionally, it is of interest to investigate if ilmenite can release the alkali when changing operating conditions, and thus enable the possibility of regenerating the material.

The aim of the present study is to characterize the desorption of alkali from ilmenite bed material previously used in an industrial scale OCAC system with biomass. This is carried out by placing alkali-containing ilmenite in a thermogravimetric analyzer (TGA) system, equipped with an on-line alkali detection instrument in the exhaust gases [39]. This setup enables us to measure the weight change and alkali release from a sample at specific temperatures and gas atmospheres. In addition, detailed material analysis is carried out on the ilmenite before and after TGA experiments to determine the abundance and distribution of key elements in the OC. The ilmenite used in this study is received from a 115 MW_{th} OCAC boiler after 225 h of biomass combustion. The material contains approximately 2 wt% K and 1 wt% Na and it has been used in another study focusing on ash interactions [22]. Although the samples used here were taken from an OCAC facility, it is expected that the results are also highly relevant for chemical looping systems.

2. Experimental

2.1. Sample extraction

The ilmenite sample used in this study was obtained from a 115 MW_{th} CFB boiler located in Örtofta, Sweden. Norwegian rock ilmenite was used as bed material. During operation, around 60 tonnes of bed and biomass waste material is present in the system. To account for losses, 15 tonnes of new bed material was added daily. The biomass fuel consisted of a 50:50 mixture of recovered waste wood and wood chips and the boiler was operated at a temperature around 850 °C [40].

The bed sample was collected from the bottom ash with a water-cooled ash extraction screw-feeder system. The sample was extracted after 225 h of operation and exposed to oxidizing conditions around 850 °C during the extraction procedure. It should be noted that since new bed material was added daily, a fraction of the extracted sample has less than 225 h exposure time in the system. The sample has been sieved to particles sizes below 710 μm to remove large pieces and magnetically separated two times to obtain an ilmenite-rich fraction [22]. Since most of the ilmenite has been present in the system for several days it contains a few weight percent of different ash components.

2.2. Sample preparation

Norwegian rock ilmenite (Titania A/S, Norway) was used for reference and was not activated prior to TGA experiments. The total elemental composition of the ilmenite samples was determined by ICP-SMFS according to the standards EN ISO 17294-2:2016 and EPA-method 200.8:1994. The composition of the reference ilmenite, is presented in Table 1, along with the composition of the ilmenite extracted from the OCAC boiler after operation for 225 h. It is clear from the table that accumulation of ash elements has occurred in the industrial process. The relative change is very large for Ca, large for K and Na, and less pronounced for Si, Al and Mn. Evident from Table 1, the OCAC ilmenite

Table 1
Composition of reference ilmenite provided by the supplier Titania A/S and ilmenite extracted after 225 h of OCAC operation in the Örtofta power plant.

wt% dry	Reference ilmenite	OCAC ilmenite
Fe	33.3	19.0
Ti	23.9	16.0
Si	0.9	4.8
Ca	0.3	10.8
Mg	1.8	2.0
Al	0.3	1.5
Na	0.1	1.0
K	0.1	1.8
Mn	0.1	0.6

contains approximately 2 wt% potassium and 1 wt% sodium.

The OCAC ilmenite particles have a mean particle diameter of 146 μm, based on the particle size distribution shown in Table 2, as determined by sieving analysis. Before TGA experiments, the samples were magnetically separated once more with a small magnet. The magnet was immersed in the sample to attract ilmenite particles and 0.5–20.3 mg was collected and placed on a TGA sample holder. The procedure increases the selectivity towards ilmenite (over e.g., ash particle contimination within the sample), which may influence the elemental composition reported in Table 1.

2.3. Experimental setup

The setup consists of a commercial TGA (Model Q500; TA Instruments), connected to a surface ionization detector (SID), see schematic in Fig. 1. The experimental setup is described in detail in a related study, where the performance is demonstrated with different types of alkali-containing samples [39]. The system allows the sample weight to be continuously monitored during online measurements of alkali leaving the sample. The TGA was operated with a constant flow of 10 ml min^{-1} N_2 balance gas and 90 ml min^{-1} of either inert (N_2) or oxidizing (synthetic air) purge gas, which flows across a platinum crucible. The crucible was shaped like a pan with a diameter of 11 mm and a raised outer edge with a height of 1 mm. Ilmenite samples with a weight between 0.5 and 20.3 mg were loaded on the sample holder and heated by 20 °C min^{-1} to 1000 °C, where they were subsequently kept at constant temperature for 10 h. Experiments following the same procedure were carried out with an empty crucible between the ilmenite experiments to quantify the background levels and ensure low alkali signal.

The alkali species leaving the ilmenite sample are transported from the TGA with the exhaust gases and fed into the SID. The exhaust gas was diluted with 600 ml min^{-1} N_2 before entering the SID. The SID detects the total alkali (K + Na) concentration in a flow with a time resolution of 1 s and the instrument has been extensively described in earlier studies [9,41].

The SID was calibrated following a previously described procedure [39], and the unit for the alkali concentrations reported in this study is at normal temperature and pressure. The reported values have also been corrected for alkali losses in the experimental system [39]. Alkali losses occur due to molecular diffusion in the TGA and aerosol particle losses in the sampling lines, and 20^{+5}_{-4}% of the alkali leaving a sample is estimated to reach the SID [39]. The uncertainty in reported absolute values is thus relatively large, while uncertainty in relative values is considerably smaller.

Table 2
Particle size distribution of 108 g OCAC ilmenite particles determined by sieving analysis.

Sieve tray hole size (μm)	Retained sample weight (g)	Fraction retained particles (%)
250	23.8	22.0
212	13.8	12.8
180	7.8	7.2
150	14.1	13.0
125	15.3	14.1
90	24.3	22.5
45	8.9	8.2
Pan	0.2	0.2

2.4. Desorption kinetic analysis

The alkali release rate, v, from a sample may be expressed by a power law:

$$v = k \bullet [Na, K]^n \quad (1)$$

where k is a rate constant, and $[Na, K]$ is the concentration of alkali species available for release from the sample. The alkali reservoir may include all alkali in the sample, but is more likely to correspond to a smaller fraction due to kinetic constraints at a given temperature. The alkali signal, I, measured by the SID is proportional to the alkali release rate v:

$$I = C \bullet v = C \bullet k \bullet [Na, K]^n \quad (2)$$

where C is an instrument-specific constant that describes the effects of several experimental parameters, including the detector function and transmission losses in the experimental system.

As shown in the Results section, the alkali release under isothermal conditions is well described by an exponential decay function:

$$I(t) = I_0 exp(-kt) \quad (3)$$

where $I(t)$ is the measured alkali intensity at time t, and I_0 is the initial intensity at time zero. Equation (3) is applied to determine k at 1000 °C in either inert or oxidizing atmosphere. The exponential decay of the experimental data shows that the release process can be described as a first order reaction, i.e. $n = 1$ in Eq. (2).

The temperature dependence of the rate constant is described by the Arrhenius equation,

$$k = A \bullet e^{-E_a/R \bullet T} \quad (4)$$

which may be expressed as,

$$\ln(k) = -\frac{E_a}{R} \bullet \frac{1}{T} + \ln(A) \quad (5)$$

where A is a pre-exponential factor, E_a is an activation energy, and R is the ideal gas constant.

The alkali intensity as a function of temperature during a temperature ramp in the TGA was analyzed to estimate the activation energy (E_a) for the alkali release. By inserting Eq. (2) into Eq. (5) and rearranging the expression becomes,

$$\ln(I) = -\frac{E_a}{R} \bullet \frac{1}{T} + \ln A + \ln[Na, K] + \ln C \quad (6)$$

where the terms ln A and ln$C$ are constants [39]. The term ln$[Na, K]$ may be assumed to be constant if the alkali release is small compared to the size of the alkali reservoir. This was concluded to be the case for oxidizing conditions but not for inert conditions (see Appendix A), and the method used to correct all data obtained in inert conditions is presented in Appendix A. Eq. (6) is used to determine E_a from the observed alkali intensity in the 900–1000 °C temperature range. Based on the experimentally determined E_a value combined with the k value determined at 1000 °C, the pre-exponential factor A is calculated using Eq. (4).

2.5. Chemical analysis of samples

To study the chemical distribution of alkali in the samples, a

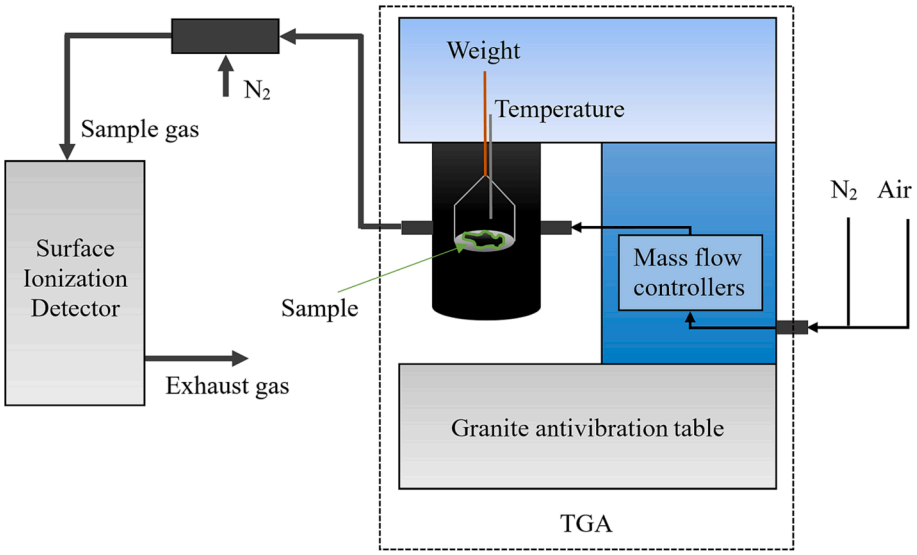

Fig. 1. Experimental setup of the SID and TGA (Model Q500; TA instruments) used for detecting alkali desorption from a sample.

scanning electron microscope (SEM), Quanta 200 ESEM FEG from FEI, equipped with an Oxford Inca energy dispersive X-ray (EDX) system was used for chemical analysis. To study the particle cross-section, samples were prepared by molding in epoxy before being polished in several steps to obtain a flat and even surface. The analysis was performed by first investigating a large area to observe trends and then gradually increasing the magnification to study individual particles. In total, three different samples were analyzed. The first sample was ilmenite as received from the OCAC power plant, while the second and third samples were ilmenite obtained from TGA experiments in inert and oxidizing atmospheres.

From the elemental maps obtained from SEM-EDX, heterogeneously mixed particles with different chemical compositions were observed and the heterogeneity is reflected in two aspects: a fraction of the particles show distinguishable elemental compositions and some elements are enriched on surfaces whereas some are only present in the cores. Chemical maps were investigated using a multivariate factor analysis technique to further study the behavior of the alkali metals. The method used is called positive matrix factorization (PMF) [42] and has been applied here to study the correlation between elements. PMF has been successfully used in many environmental and chemometric evaluation applications [43] and the function of the PMF is to identify factors that can describe common features between elemental maps. The open-source software EPA PMF 5.0 is used here for the data treatment [44]. Chemical maps are digitized using MatLab creating an excel file which is used as input in EPA PMF 5.0. Before running the program, the number of factors need to be chosen. As with other types of factor analysis the number is chosen based on knowledge about the sample characteristics. Due to complex distribution of elements in this specific case, different numbers of factors were investigated and it was concluded that three factors provide results with physical meaning for the overview images, while four factors were used for images with higher magnification. Further details of this procedure is described elsewhere [45].

X-ray Photoelectron Spectroscopy (XPS) was used to study the outermost layer of the ilmenite particles. The PHI 5000 VersaProbe III Scanning XPS Microprobe was used with a monochromated Al-source (25 W) along with dual-beam charge neutralization for charge compensation during measurements. Analysis points were specified using x-ray induced secondary electron imaging. Data was collected using a 100 μm beam size and pass energy of 224 eV and 26 eV for survey and region scans, respectively. Region spectra were collected for C 1s, O 1s, S 2p, Na 1s and K 2p. Charge referencing was made to the adventitious C 1 s line at 284.8 eV. The peak areas of each element were normalized by the atomic sensitivity factors (ASF) provided by the Multipak software in the quantitative analyses of the surface composition. The survey spectra were used to quantify the surface composition. Region spectra were analyzed using the Multipak software and peak positions were compared with literature [46].

3. Results

The main experimental results consist of alkali concentration and mass loss profiles from ilmenite OC samples in either inert or oxidizing environments at temperatures up to 1000 °C. Experiments were carried out with different sample amounts and the alkali desorption profiles were further analyzed to determine the Arrhenius parameters activation energy E_a and pre-exponential factor A. The main results are presented in the following four sub-sections including results from complementary analyses of the ilmenite samples in Section 3.4.

3.1. Alkali desorption and sample mass loss in inert and oxidizing conditions

Fig. 2a and b shows the alkali desorption and sample mass profiles from 13 mg ilmenite samples during TGA temperature ramps, where the effect of different environments is compared. The alkali desorption in Fig. 2a shows a substantial alkali peak between 630 and 800 °C in both oxidizing and inert environments. This low temperature alkali desorption likely originates from loosely bound alkali that condenses at the surface of the particles during sample extraction from the industrial process. As the temperature rises further a second alkali release starts around 900 °C, which increases in intensity as the temperature approaches 1000 °C and continues during the subsequent period with isothermal conditions. The desorption kinetics depend on the oxygen activity at 1000 °C, where the alkali signal shows a more rapid decay in inert atmosphere compared to oxidizing atmosphere. The normalized sample mass profiles are shown in Fig. 2b. The sample weight decreases at high temperatures, with a more rapid weight loss in the inert environment compared to the oxidizing environment, indicating that the gas composition has a significant influence on the stability of the ilmenite sample. Similar mass loss and alkali desorption profiles from additional experiments on the same ilmenite material, including data for the first alkali peak, can be seen in Figure A.1 in Appendix A.

The total amount of alkali released by the ilmenite can be estimated by integrating the SID signal over time. The alkali released from the ilmenite samples are 1.27 and 2.87 g kg^{-1} sample in inert and oxidizing

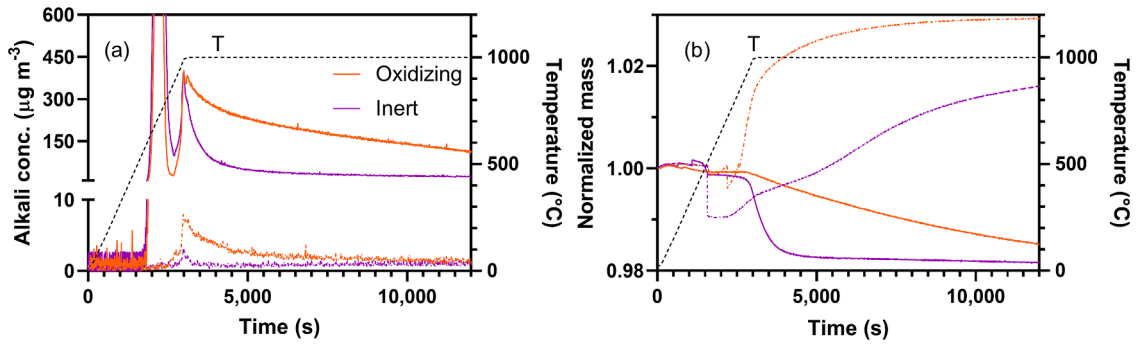

Fig. 2. Alkali desorption profiles and normalized mass profiles obtained in experiments with: (solid lines) ilmenite received from the OCAC power plant, and (dashed lines) unused reference ilmenite. Results from experiments carried out in inert (purple) and oxidizing (orange) atmospheres are displayed. (For interpretation of the references to colour in this figure legend, the reader is referred to the web version of this article.)

atmospheres, respectively, considering the 100 ml min^{-1} flow rate through the TGA and assuming an alkali transmission transmission of 20% between the TGA and the SID [39]. The alkali content in the ilmenite prior to TGA experiments is 27.8 g kg^{-1} (Na + K in Table 1). Thus, only 4.6 wt% and 10.3 wt% of the available alkali content is released from the ilmenite in inert and oxidizing atmosphere, respectively. Considering only the second, high temperature alkali release starting from 900 °C, the total amount of alkali released from the ilmenite samples are 0.89 and 2.53 g kg^{-1} sample (corresponding to 3.2 and 9.1 wt% of the available alkali) in inert and oxidizing atmospheres, respectively.

Fig. 2a and b also shows the corresponding alkali desorption and mass loss profiles during TGA temperature ramps for reference ilmenite samples that have not been used in the combustion process. The reference ilmenite does not show the early alkali desorption peak and the alkali release is limited under isothermal conditions. This implies that the unambiguous alkali release seen from the OCAC ilmenite originates from alkali added to the ilmenite during biomass combustion and not from the ilmenite material itself. Since the reference sample is received in its reduced form, it gains weight in oxidizing atmosphere at high temperatures (Fig. 2b). However, the reference sample is gaining weight in the inert atmosphere as well, indicating that some amount of oxygen slips into the TGA during experiments. The oxidation rate is significantly higher in the oxidizing atmosphere compared to the inert atmosphere. Therefore, the inert environment may be considered a *low oxygen activity* environment instead of a completely *inert* environment. In contrast to the reference ilmenite sample, the ilmenite taken from the industrial process experienced oxygen partial pressures between 0.21 and 0.04 during OCAC operation [23], and does not gain oxygen during the TGA experiments.

The TGA-SID experiments were conducted with different sample amounts loaded on the TGA sample holder to evaluate the influence of sample size on alkali release.

Fig. 3 shows alkali desorption profiles for initial sample masses varying from 0.5 to 20.3 mg in an inert atmosphere and from 1.2 to 12.9 mg in an oxidizing atmosphere. Fig. 3a shows the alkali desorption increases with increasing sample size in the inert atmosphere. This is true for both the loosely bound alkali leaving at lower temperatures and the alkali desorbing at higher temperatures. Fig. 3b shows the corresponding alkali desorption curves normalized to the height of the second peak (at 1000 °C). The normalized curves show that the decay in alkali concentration along the isotherm is steeper for smaller sample sizes. This is

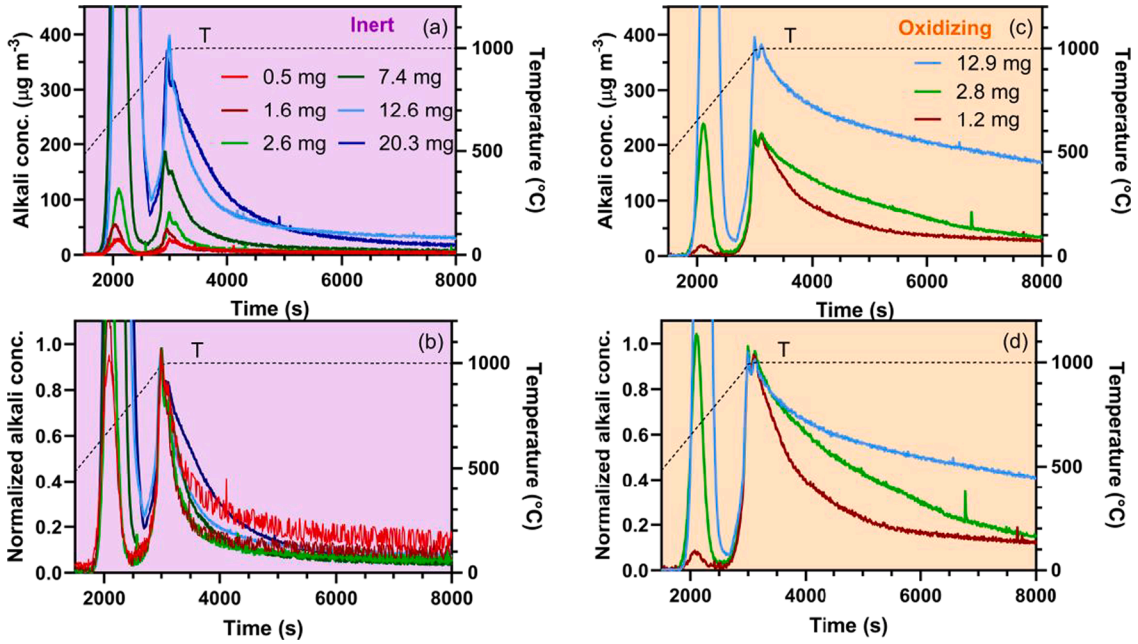

Fig. 3. Changes in alkali desorption with ilmenite sample size varying between (a and b) 0.5 and 20.3 mg in inert conditions, and (c and d) 1.2 to 12.9 mg in oxidizing conditions. The two upper panels (a and c) show the absolute alkali levels and the two lower panels (b and d) show the corresponding alkali levels normalized to the height of the second peak. The dashed line shows the temperature.

true for all sample amounts between 1.6 and 20.3 mg, with an exception for the smallest sample size (0.5 mg) where the decay is initially rapid but slows down after approximately 100 s.

Fig. 3c and d shows the corresponding alkali desorption profiles for sample masses between 1.2 and 12.9 mg in an oxidizing atmosphere. The change in sample size in an oxidizing atmosphere shows a similar dependence as in the inert environment. The alkali concentration decreases more rapidly for smaller sample sizes, indicating that the observed kinetics are influenced by the amount of sample used in the experiments.

3.2. Alkali desorption and mass loss kinetics under isothermal conditions

Mass loss and alkali desorption profiles for two sample sizes in both inert and oxidizing atmospheres are shown in Fig. 4, together with fits of the experimental results with exponential decay functions. The alkali results are fitted using Eq. (3) and the weight data are treated by a corresponding procedure. The mass and alkali profiles in Fig. 4a, c and d are fitted from the point when the temperature has stabilized at 1000 °C (*i.e.* between 3000 and 8000 s experimental time). For Fig. 4b, the mass loss profile was fitted between 3000 and 3800 s, since the mass began to increase after 3800 s. A single exponential function represents the experimental data relatively well, which indicates that the alkali desorption and mass loss both follow first order kinetics.

The rate constants determined for all investigated cases are summarized in Table 3 and presented as a function of sample size in Fig. 5. Fig. 5a shows that the rate constants for both alkali and weight increase with decreasing sample size under inert conditions, where the 0.5 mg case is treated as an outlier and hence not included in the linear regression. The weight rate constant in oxidizing atmosphere also increases with decreasing sample size in oxidizing atmosphere, while no clear trend is seen for the alkali release rate constant (Fig. 5b). In addition, the alkali desorption rates are 3–7 times higher in the inert atmosphere compared to the oxidizing atmosphere. A remarkable feature is the similarity between the rate constants for weight loss and alkali desorption. The observed mass loss is substantially larger than the amount of released alkali (see *e.g.* Fig. 2b where 2.6 μg of alkali desorb and 200 μg mass is lost between 3000 and 5000 s in inert atmosphere). Hence, the alkali loss only makes a minor contribution to the observed sample mass loss, but the alkali release is likely to be affected by the process responsible for the sample mass loss.

Table 3
Rate constants (k, in s^{-1}) for alkali desorption and sample weight loss at 1000 °C. Error limits are 95% confidence intervals.

Sample In/Ox (mg)	Inert		Oxidizing	
	Alkali (s^{-1} •10^{-5})	*Weight* (s^{-1} •10^{-5})	*Alkali* (s^{-1} •10^{-5})	*Weight* (s^{-1} •10^{-5})
0.5	189 ± 4.0			
1.6/1.2	392 ± 5.9		74 ± 1.1	54 ± 1.8
2.6/2.8	317 ± 3.6	493 ± 6.7	46 ± 0.3	76 ± 0.5
7.4	222 ± 1.1	349 ± 1.6		
12.6/12.9	201 ± 1.4	217 ± 1.1	42 ± 0.5	10 ± 0.1
20.3	120 ± 0.4	185 ± 0.3		

The rate constant results obtained in inert conditions may be described by a linear dependence on initial sample weight (Fig. 5a). If a linear relationship is assumed and the regressions are extrapolated to zero mass, the rate constants for alkali desorption and weight equals $3.7•10^{-3}$ s^{-1} and $5.0•10^{-3}$ s^{-1} respectively. Larger samples have a larger surface area available that can interact with the desorbed alkali, which may lead to mass transfer limitations and consequently a change in the observed desorption rate constants. One may, therefore, consider the desorption rates from the "zero mass" extrapolations to be more representative since they are less affected by mass transfer limitations.

Changing sample size in the oxidizing atmosphere did not change the rate constants for alkali and weight as much as they did in the inert atmosphere. Since oxidizing atmosphere is only applied in three experiments, it is more difficult to establish "zero-mass" desorption rate constants for this environment. With that in mind, if we assume a linear relationship and extrapolate to represent "zero mass", the desorption

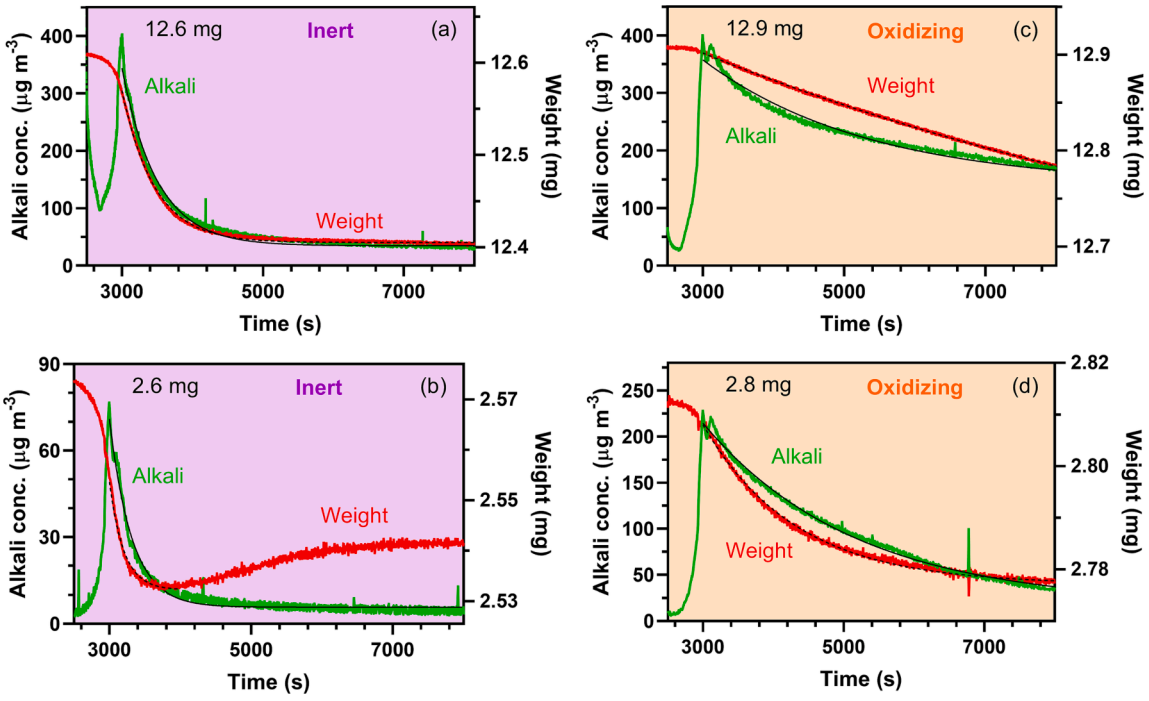

Fig. 4. Sample mass loss and alkali desorption profiles and their corresponding exponential decay functions at a constant temperature of 1000 °C in (a and b) inert conditions and (c and d) oxidizing conditions. Alkali levels are visualized with solid green lines, sample weight with solid red lines, exponential decay function for alkali solid black lines and exponential decay function for sample mass with dashed black lines. (For interpretation of the references to colour in this figure legend, the reader is referred to the web version of this article.)

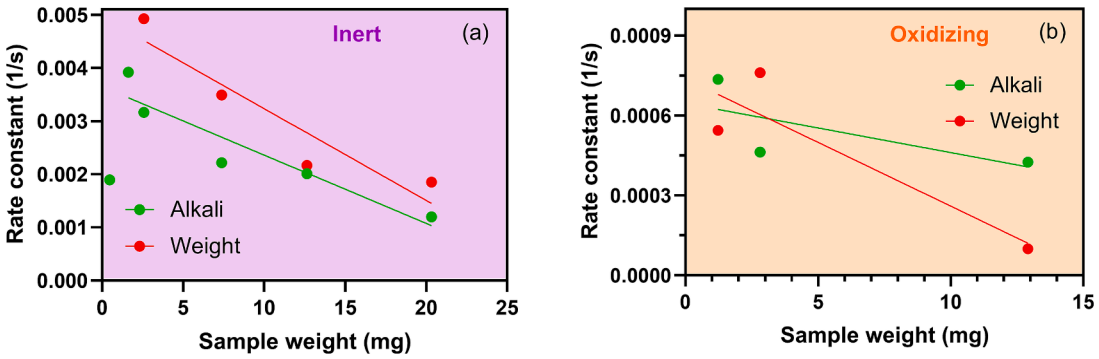

Fig. 5. Desorption rate constants (k, in s^{-1}) for alkali desorption and sample weight at 1000 °C.

rate constants for alkali and weight in oxidizing conditions are $6.5 \bullet 10^{-4}$ s^{-1} and $7.4 \bullet 10^{-4}$ s^{-1} respectively.

3.3. Temperature dependence of alkali desorption kinetics

Fig. 6 shows the measured alkali concentration, *I*, as a function of 1/T in the temperature range from 900 to 994 °C. The figure compares cases with 2.6 and 2.8 mg sample mass in an inert and oxidizing environment, respectively, and the solid black lines represent ln(*I*) calculated from Eq. (6).

The Arrhenius parameters for the two cases are determined from ln (*I*) in Eq. (6) and they are summarized in Table 4 together with the Arrhenius parameters for all other sample masses. In an oxidizing environment, both E_a and *A* increase with decreasing sample mass. The case with the smallest sample mass (1.2 mg) has a pre-exponential factor of $1 \bullet 10^{12.4 \pm 0.1}$ s^{-1}, which is close to the typical value of $1 \bullet 10^{13}$ s^{-1} for an ordinary first-order desorption process [47]. This indicates that the

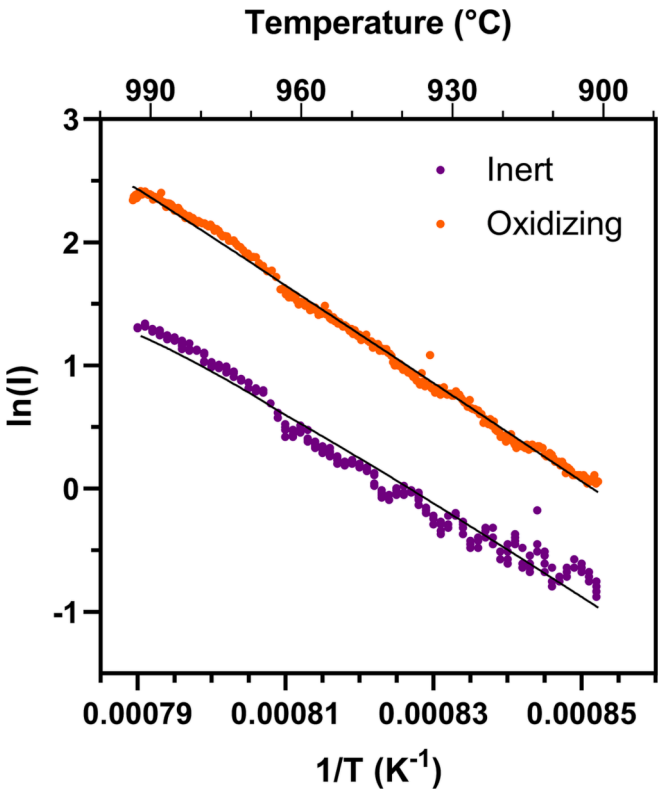

Fig. 6. Logarithmic alkali signal intensity over 1/T in the temperature ramp between 900 and 994 °C for ilmenite samples in inert conditions and oxidizing conditions. Black lines show ln(I) described by Eq. (6).

Table 4
Arrhenius pre-exponential factors (A, in s^{-1}) and activation energies (E_a, in kJ•mol^{-1}) for different ilmenite sample sizes in inert and oxidizing atmospheres. The 95% confidence intervals of A and E_a are included in the table.

Sample In/Ox (mg)	Inert		Oxidizing	
	A	E_a	*A*	E_a
0.5	$1 \bullet 10^{7.5 \pm 0.4}$	250 ± 10		
1.6/1.2	$1 \bullet 10^{10.9 \pm 0.3}$	323 ± 7	$1 \bullet 10^{12.4 \pm 0.1}$	378 ± 3
2.6/2.8	$1 \bullet 10^{11.0 \pm 0.2}$	329 ± 6	$1 \bullet 10^{10.4 \pm 0.1}$	334 ± 2
7.4	$1 \bullet 10^{10.4 \pm 0.2}$	317 ± 5		
12.6/12.9	$1 \bullet 10^{5.9 \pm 0.2}$	209 ± 4	$1 \bullet 10^{7.9 \pm 0.1}$	275 ± 3
20.3	$1 \bullet 10^{6.3 \pm 0.3}$	224 ± 6		

observed kinetics are determined by the desorption process and the obtained activation energy of 378 ± 3 kJ mol^{-1} may be associated with the binding energy between alkali and the surface. For larger sample sizes the kinetics are affected by mass transfer limitations within the samples, which results in lower E_a and *A* values. In an inert environment, the trends are less clear with *A* values between $1 \bullet 10^{11.0 \pm 0.1}$ and $1 \bullet 10^{10.4 \pm 0.1}$ s^{-1} and E_a values in the 317–323 kJ mol^{-1} range between 1.6 and 7.4 mg sample masses. The smallest sample, 0.5 mg, may again be treated as an outlier with a noisy alkali signal and low *A* and E_a values. The two largest samples, 12.6 and 20.3 mg, have generally lower *A* and E_a values around $1 \bullet 10^{6.1}$ s^{-1} and 217 kJ mol^{-1}, respectively.

There are three cases of comparable masses that are studied in both oxidizing and inert environments. In general, both *A* and E_a are lower in the inert environment than in the oxidizing environment for samples with comparable mass. The only exception is a slightly higher *A* at 2.6 mg in the inert environment compared to 2.8 mg in the oxidizing environment.

3.4. Material analysis

Ilmenite particles were also studied using SEM-EDX and XPS before and after TGA experiments, to investigate the alkali distribution and changes in chemical properties. XPS was used to study the outermost surface while SEM-EDX was used to investigate the alkali distribution among and along the particle cross-sections. To distinguish the behavior between K and Na, chemical mappings produced by SEM-EDX were further processed using PMF.

3.4.1. Ilmenite prior to TGA experiments

The cross-section of the ilmenite sample and corresponding chemical maps are presented in Fig. 7. Chemical maps were first obtained over a large area to observe the overall trends in composition Fig. 7a. Areas in Fig. 7b and c where Fe and Ti overlap are identified as ilmenite particles. A major amount of Ca is present both inside and on the surface of these particles. The total composition is presented in the table and it can be observed that Ca and Si are the major ash elements. It is also evident that

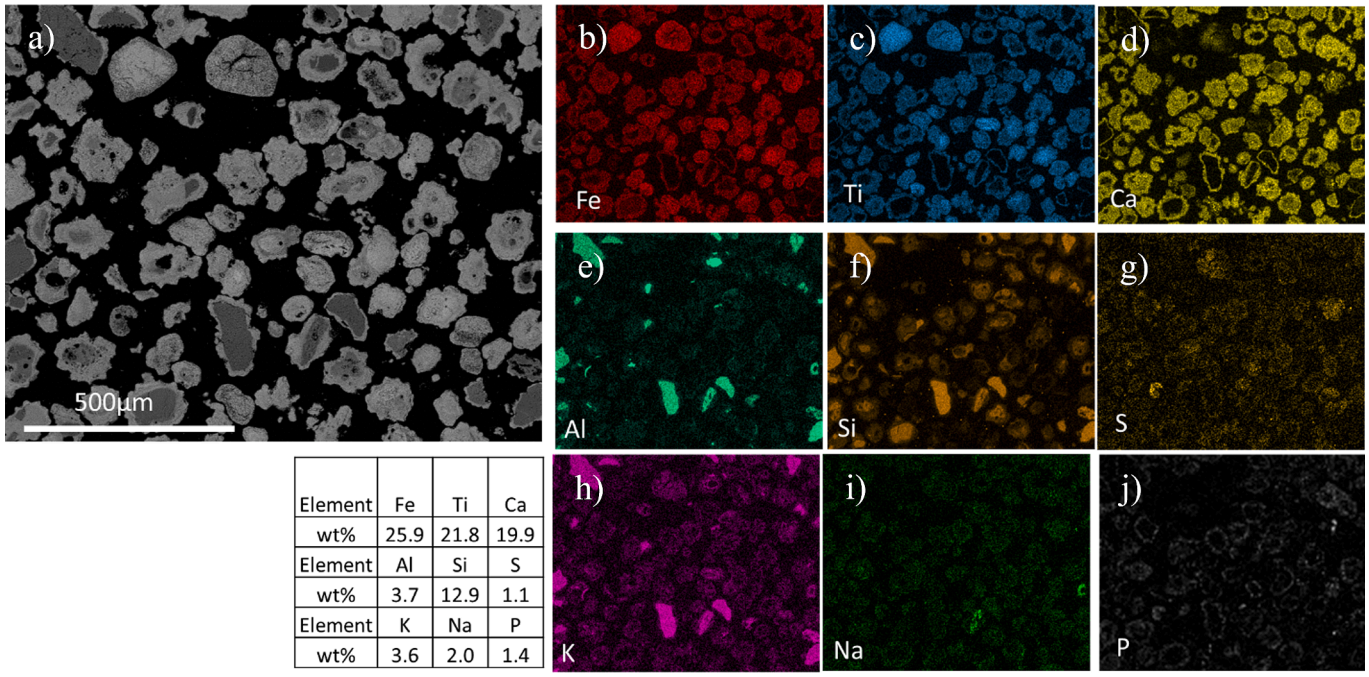

Element	Fe	Ti	Ca
wt%	25.9	21.8	19.9
Element	Al	Si	S
wt%	3.7	12.9	1.1
Element	K	Na	P
wt%	3.6	2.0	1.4

Fig. 7. (a) Micrograph of the cross-section of ilmenite sample. (b-j) Chemical maps of the major components of ilmenite (Fe and Ti), major ash elements (Ca, Si) along with Al, P and the alkali species (K and Na). The total content in weight percent is presented in the table (excluding C and O).

the elements K, Al and Si overlap. Point analyses on a few of these types of particles all showed that the relation between the elements K:Al:Si is approximately 1:1:3 on molar basis, well aligned with the composition of potassium feldspar $KAlSi_3O_8$. The silicates could have been present in the boiler from the start, added from the fuel and/or originating from impurities in the ilmenite material.

To further investigate the correlation between the elements, the digital chemical maps of all elements were processed by PMF. The result from the PMF analysis is presented in Fig. 8, where three factors are resolved. The factor profile (Fig. 8e) shows the elemental compositions of each factor. Factor 1 is dominated by Fe and Ti, which is the feature of ilmenite particles. The primary composition of Factor 2 is Ca, followed by Fe, Ti and Si, which indicates that this factor is associated with a mixture of ilmenite and ash elements. Factor 3 is strong in K, Si and Al, well in line with the potassium feldspar chemical composition.

Based on the PMF factor distribution, the calculated map of each factor is obtained and plotted in Fig. 8b–d. In these images, high intensity is proportional to a high correlation with the specific factor. For example, in Fig. 8b the bright areas are featured by Factor 1 rich in iron and titanium, which are primarily ilmenite particles. These are likely newly fed into the OCAC boiler and have not had time to interact with the ash components. These particles are typically larger, *e.g.* the two bright particles in the top left corner in Fig. 8b. Factor 2 identifies areas that are rich in ash components, especially Ca. Highlighted regions in Fig. 8c include ash coatings on feldspar particles, as well as ilmenite particles with a longer residence time. Factor 3 particles highlighted in Fig. 8d are feldspar particles, which have relatively well-defined boundaries. All feldspar particles have a coating layer, observed in Fig. 8c, in accordance to previous studies [48]. The potassium is mainly associated with Factor 3, *i.e.*, in the form of potassium silicate, likely feldspar. Sodium, on the other hand, correlates with all three factors.

A line scan across the ash layer in an ilmenite particle is marked in

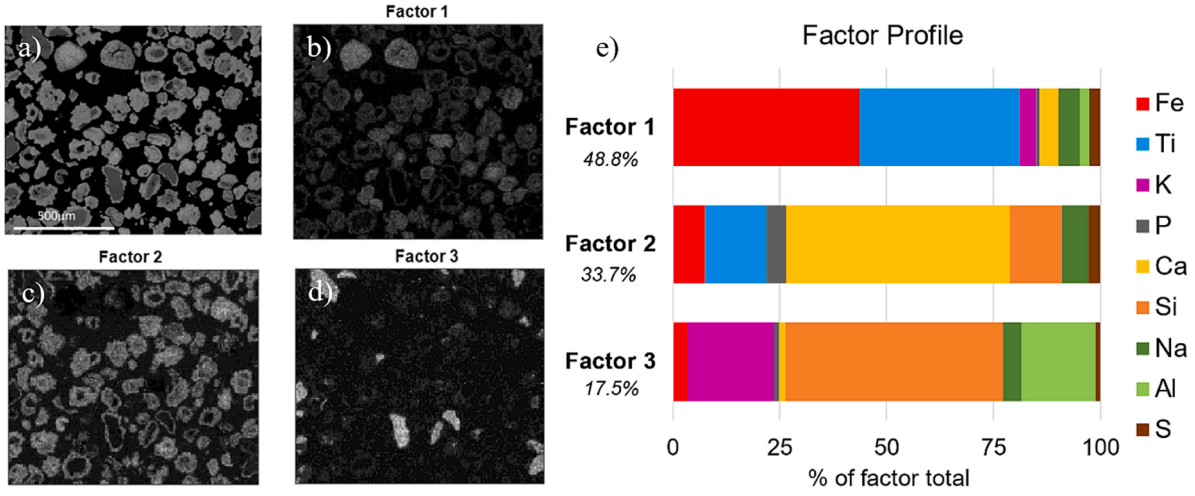

Fig. 8. (a) Micrograph of ilmenite sample along with (b-d) factor intensities. (e) Fraction of each factor in the sample and elemental contribution to each factor profile.

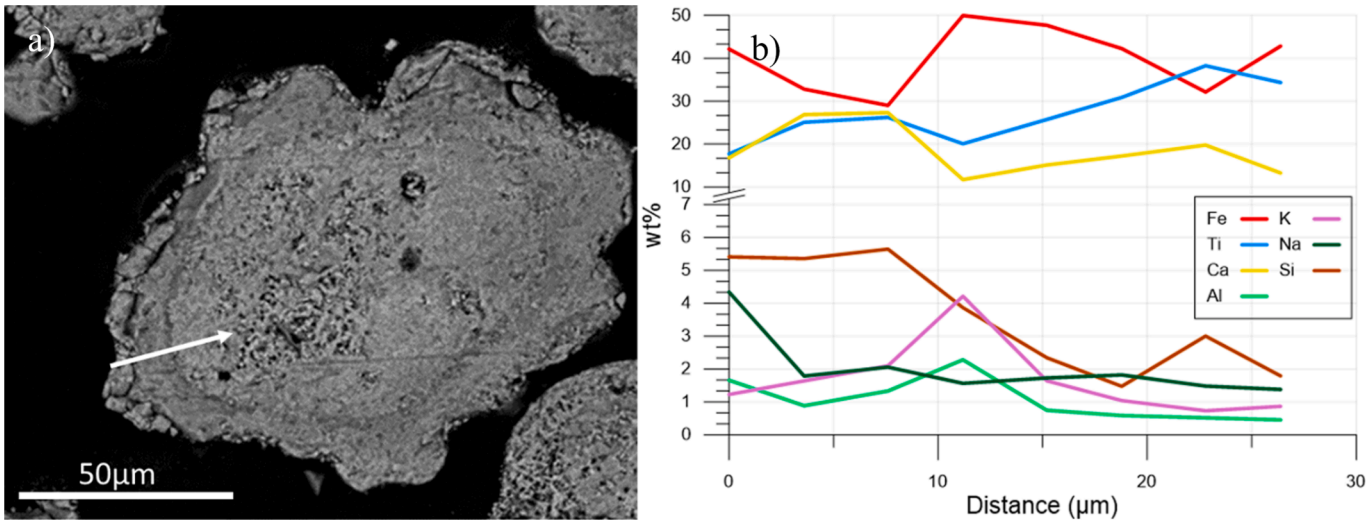

Fig. 9. Line scan performed over the ilmenite particle ash layer. (a) The white arrow in the micrograph indicates the start and direction of the line scan. (b) The elemental composition in weight percent at 11 points along the line scan.

Fig. 9a, and the elemental density profiles along the arrow are shown in Fig. 9b. The major elements are Ca, Fe and Ti, and the minor are Al, Si, K and Na. The profile shows that the Na concentration is higher at the particle surface, while K is concentrated deeper into the particle (at 11 µm in Fig. 9) and found at the interface between the ilmenite and an outer ash layer rich in Ca, in accordance with previous ilmenite studies [11,22]. The corresponding chemical maps and factor profiles for the individual particle shown in Fig. 9 can be found in Appendix A, Figures A.3 and A.4.

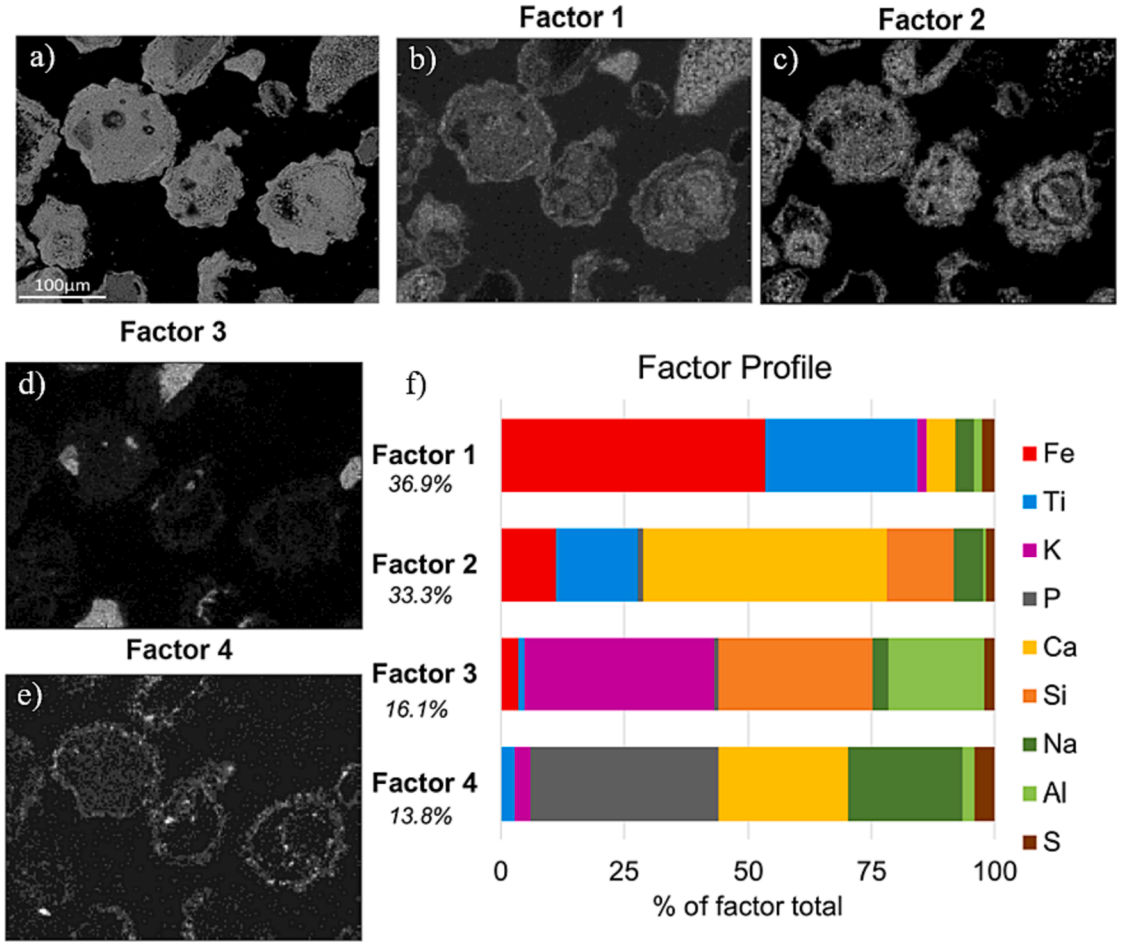

Fig. 10. (a) Cross-section micrograph of ilmenite sample exposed to inert conditions at 1000 °C for 10 h, along with (b-d and f) PMF factor intensities. (e) Fraction of each factor in the sample and elemental contribution to each factor profile.

3.4.2. Ilmenite obtained after TGA experiments

The micrograph and PMF factor profiles for the cross-section of an ilmenite sample, obtained after 10 h TGA experiments in inert atmosphere at 1000 °C, are presented in Fig. 10. In the PMF analysis, factors 1–3 (Fig. 10b–d) remain similar in composition as previously described. A fourth factor was added, featured as coatings (Fig. 10e) containing P, Na and Ca. These three elements are enriched on the particle surfaces, also observed in Figs. A.9–A.11 in Appendix A. The PMF analysis (Fig. 10f) shows correlation between Ca, Na and P. These phosphates are located closer to the surface and enriched in small spots in the particle ash layer. Since these phosphates are observed both before and after TGA experiments it is assumed that they remain stable compared to other compounds which may be present. The results from the TGA experiments in an inert atmosphere were similar to those in an oxidizing atmosphere (see Appendix A Figs. A.5–A.11). The results are consistent with a recent thermodynamic analysis of the fate of ash elements when ilmenite is used as an oxygen carrier, which showed that Na is more inclined to form phosphates while K is more likely to be found in the form of titanates [49].

3.4.3. Material surface analysis

The topmost surface of the ilmenite particles was further investigated with XPS. The relative elemental concentrations on the surface before and after exposure to inert and oxidizing conditions are presented in Fig. 11. Fe, Ti and Ca are the major elements on the ilmenite surface. The alkali metals K and Na are both present, and Na has a slightly higher concentration in comparison to K. Previous studies investigating the same type of ilmenite samples with XPS have reported similar results, with higher concentrations of Na at the outermost particle surface in comparison to K [23]. The region spectra for Na 1s and K 2p show broad peaks with components located at different binding energies indicating that the alkali metals are present in several chemical states, including oxides, chlorides and sulfates. The region spectra of S 2p confirmed the presence of SO_4^{2-}. Region spectra of Na 1 s, K 2p and S 2p can be found in Figure A.12 in Appendix A.

One noticeable difference in the surface composition for ilmenite particles before and after TGA experiments (Fig. 11) is that the latter has more Ca on the surface. During the TGA experiment, Ca accumulates on the surface of the particles, which explains the lower levels of Fe and Ti. Another interesting difference between particles before and after TGA experiment is that the latter has less S and Cl at the surface. Based on this information it is likely that alkali left the ilmenite sample in the form of alkali chlorides during the TGA experiments. The difference in sulfur may be due to desorption of alkali sulfates, but a more likely scenario is differences in $CaSO_4$ concentrations on the surface.

Ilmenite samples after TGA experiments in inert and oxidizing atmospheres were further investigated using sputter etching to study the chemical composition at different depths. Sputtering was performed using an Ar^+ beam (2.0 kV) which was rastered over a 3 × 3 mm^2 area. The etch rate, with respect to Ta_2O_5, is 49.0 Å/min corresponding to a total depth of 16 nm in the experiments. The surface composition obtained after sputtering is presented in Fig. 12. Again, almost no Cl is present at the outermost particle surface after TGA experiment in both the inert and oxidizing environments, but a significantly higher concentration of Cl was observed at 16 nm depth for the particles from the inert environment, compared to those from the oxidizing. This implies that alkali and Cl may have left the sample from a deeper layer in the oxidizing environment compared to the inert environment. They might either diffuse as alkali chlorides or independently before combining and desorbing at the surface. This is in line with the experimental results (see Fig. 2) where a larger amount of alkali leaves the sample under oxidizing conditions. Another interesting feature in Fig. 12 is that Fe and Si are replacing each other. The outermost surface contains more Si compared to what is present at 16 nm depth, and the reverse can be said about Fe.

4. Discussion

4.1. Alkali interactions with ilmenite

Ilmenite is considered to be a benchmark OC for chemical looping and OCAC systems. The present study clearly shows that ilmenite samples used for OCAC of biomass release alkali in both inert and oxidizing environments at high temperatures.

Previous studies have reported interactions between ilmenite and biomass ashes from a 12 MW_{th} plant operated under OCAC conditions [11,25]. The authors used several material analysis methods, including SEM-EDX, X-ray diffraction and X-ray fluorescence, to study the ash layer properties and migration mechanisms in ilmenite samples. However, the studies focused on the interactions induced by K and Ca but did not consider Na. Studies show that both K and Ca migrate inwards to form products with titanium oxides, as Fe simultaneously migrates

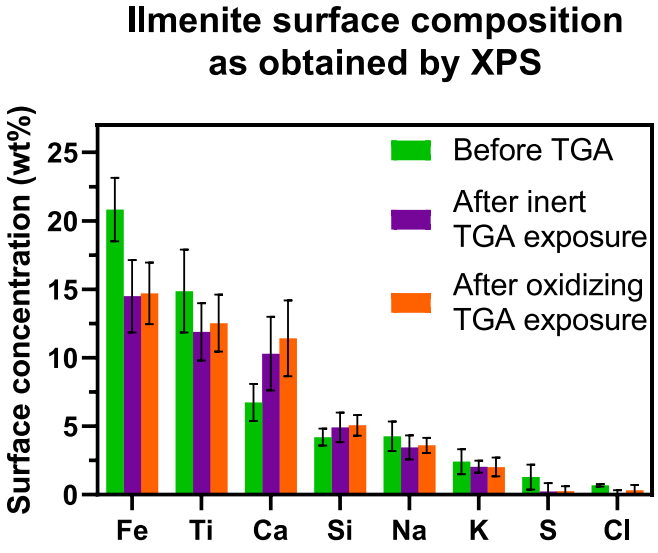

Fig. 11. Summary of the surface composition of ilmenite particles obtained by XPS for samples before TGA experiment and after TGA experiments in both inert and oxidizing atmospheres at 1000 °C for 10 h.

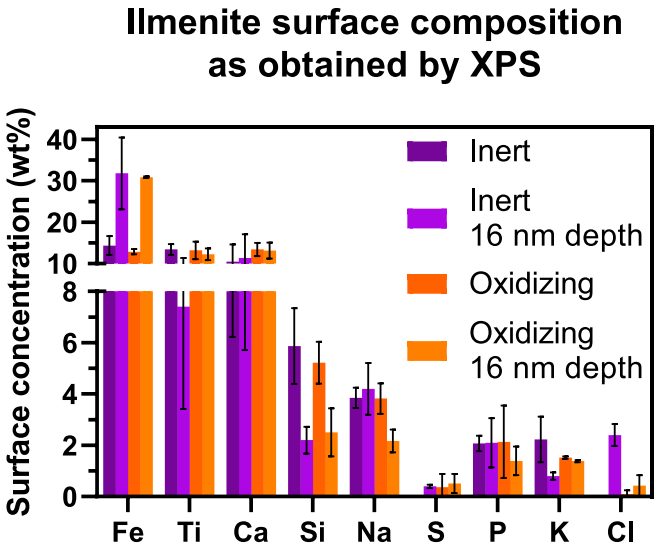

Fig. 12. Surface composition of ilmenite particles obtained by XPS. Composition is obtained at 16 nm depth generated by sputtering, and compared with the outermost surface composition. Samples obtained after TGA experiments in inert and oxidizing atmospheres at 1000 °C for 10 h.

outwards [25]. The segregation between Fe and alkali is more commonly realized as alkali roasting which is used in industries to refine TiO_2 from ilmenite. Here K_2CO_3 and NaOH are used to improve the separation between Fe and Ti [36]. The procedure enables alkali to react with Fe and Ti separately, dividing the combined ilmenite into one phase of alkali-iron oxide and one phase of alkali-titanium oxide. The ash migration seems more rapid for K compared to Ca and accumulation of Ca, together with other elements like Si and P, can be found on the surface of the ilmenite particles while the outer ash layer does not include K [11]. Furthermore, it was found that less than 1 wt% of the total K-content in ilmenite could be leached. It is believed that this corresponds to the K that had not yet formed the product KTi_8O_{16} [25].

During biomass conversion in a 100 kW CLC pilot using an ilmenite rich OC, high concentrations of alkali were detected in the product gases leaving the air reactor [29]. Since no fuel is present in the air reactor, the alkali must have been transported there, either directly as ash particles or with the OC. A possible scenario is that alkali is adsorbed by the OC in the reducing atmosphere of the fuel reactor, and desorbed from the OC in the oxidizing atmosphere of the air reactor which often operates at a higher temperature. Since the alkali detection system cannot distinguish between K and Na, the alkali found in the product gases leaving the air reactor could be any of the two or a combination of both.

The present study shows that despite rather low alkali desorption in contrast to the total amount available in the sample, the total desorption above 900 °C is considerably larger under oxidizing conditions compared to inert conditions (9.1 wt% and 3.2 wt% of the available alkali amount respectively). The TGA experiments show two clear alkali desorption stages. The first stage is seen between 630 and 800 °C and the second stage begins at 900 °C. The low-temperature desorption process shows no clear dependence on oxygen activity and probably originates from loosely bound alkali on the surface of the particles. Since the OCAC power plant operates at temperatures around 850 °C, the alkali leaving the sample below 800 °C likely originates from the sample extraction process. These low-temperature interactions would probably not take place inside the combustion unit during operation.

The second, high-temperature, alkali desorption stage shows a clear environmental dependence. At a temperature of 1000 °C, the alkali emission is higher in oxidizing atmosphere compared to inert atmosphere. This is in line with the findings in a 100 kW CLC study where large alkali concentrations were detected after the air reactor [29], suggesting that ilmenite may release alkali in oxidizing environments. In this study, it was observed that the Cl concentration at 16 nm depth of the ilmenite particle surface is lower after TGA experiments in oxidizing conditions compared to inert, see Fig. 12. If alkali is released as chlorides (NaCl or KCl) from a deeper level in an oxidizing atmosphere, it explains the higher alkali desorption in the oxidizing atmosphere.

It is difficult to determine if Na, K, or a combination of both, is responsible for the alkali desorption profiles. Future experiments would benefit greatly if the SID could identify K and Na separately. A new study has recently been published where the authors used a rapidly reversing field potential between the ion source and the collector plate inside the SID, which can be used to distinguish K and Na due to their differences in surface desorption kinetics [50]. In this study, a significant amount of the K in the sample is associated with silicates, with an elemental composition like potassium feldspars ($KAlSi_3O_8$), see Fig. 7. These silica compounds are considered inert with respect to alkalis in this study since they most likely absorb K during biomass combustion until they are saturated after which they are assumed not to release any alkali. Although some K was found on the outermost surface of the ilmenite particles, higher K concentrations were found at a deeper level, *approx.* 11 μm into the particle, coated by ash layers rich in Ca. In comparison, Na correlates with ilmenite, silicates and other ash components. Significant Na concentrations are found at the outermost surface of the ilmenite particles. The surface concentration of K and Na, together with Cl, are lower at the ilmenite surface after the TGA experiments.

4.2. Implications for chemical looping and OCAC studies

Alkali is readily released during the conversion of biomass and it is of great importance to develop an understanding of the fate of alkali in the process to avoid devastating problems like bed agglomeration and corrosion of process equipment. Based on the findings in this study, ilmenite samples that consist of 2 wt% K and 1 wt% Na release alkali to some extent in conditions relevant for OCAC, CLC and other thermal conversion systems.

The 115 MW_{th} OCAC boiler that provided the ilmenite used in this study was operated at 850 °C, and the observations in this study are mostly related to an alkali fraction that is less mobile at 850 °C and released at higher temperatures. There is another alkali fraction that is active and released below 850 °C which may be related to the alkali peak at low temperatures in these experiments. However, majority of the alkali desorption from this material begins at temperatures above 900 °C. In the OCAC boiler, the OC and ash are exposed to temperature gradients which may occur due to hot spots in sections of the fluidized bed. Furthermore, CLC usually operates at higher temperatures with more clear atmospheric differences. The fuel reactor in a CLC system generally operates around 970 °C in a reducing atmosphere, while the air reactor operates in an oxidizing atmosphere at temperatures up to 1050 °C [51]. The studied alkali desorption profiles show that ilmenite releases alkali at temperatures relevant for CLC with higher desorption in oxidizing atmosphere (conditions relevant for the air reactor) compared to inert atmosphere (conditions relevant for the loop-seals). Since most of the heat extraction occurs in proximity to the air reactor of a CLC system, it is of great importance to establish an understanding of the desorption mechanisms under these operating conditions to reduce fouling and corrosion of heat exchanger surfaces.

In OCAC, the OC particles will endure reducing atmospheres in areas with high fuel concentrations. In a similar fashion, the fuel reactor of a CLC process also operate under reducing conditions. It would, therefore, be valuable to study alkali release from the ilmenite samples in a reducing atmosphere, which has not been considered in this study.

5. Conclusions

Experiments have been carried out to study the desorption of alkali from ilmenite OC material previously used during OCAC of biomass. The TGA-SID setup was proven successful in measuring alkali desorption from the OC sample under inert and oxidizing conditions at temperatures up to 1000 °C. In addition, detailed material analyses were performed on the ilmenite before and after TGA experiments with SEM-EDX and XPS. The main conclusions can be summarized as follows:

- The ilmenite received from the 115 MW_{th} OCAC process contains 2 wt% K and 1 wt% Na. The samples release alkali in both inert and oxidizing environments with a total amount of *approx.* 4.6 wt% and 10.3 wt% of the available alkali amount respectively. The alkali desorption profiles can be separated into two periods. The first occurs around 630–800 °C independent of oxygen activity, and the second above 900 °C where the total alkali desorption is larger in the oxidizing atmosphere compared to inert.
- Arrhenius parameters, activation energy (E_a) and pre-exponential factor (A), are determined. The dependence on sample mass and effects of inert/oxidizing environments are presented. When more sample mass is involved, the observed alkali desorption is most likely affected by mass transfer limitations within the samples. A relatively simple and close to first-order desorption is observed in the oxidizing environment, with a pre-exponential factor of *approx.* $1 \bullet 10^{12.4 \pm 0.1}$ s^{-1} and an activation energy of 378 ± 3 $kJ \bullet mol^{-1}$. In an inert environment, the alkali release is apparently more complex than that in an oxidizing environment.
- The material analyses showed that significant amounts of K exist as potassium feldspars that are stable during TGA experiments. Some K

was found on the outermost surface of the ilmenite particles, while larger amounts were found at the interface between the ilmenite and a Ca-rich ash layer. The Na coexists with phosphorous, ilmenite and feldspars, and significant amounts of Na are found on the outermost surface of ilmenite particles. The surface concentration of both K and Na decreases, together with Cl, during TGA experiments. The Cl is depleted from a deeper layer in an oxidizing environment compared to an inert environment.

Several future experiments could be helpful to develop a deeper understanding of the alkali desorption process. Maybe the most interesting, concerning chemical looping studies, is to conduct the TGA experiments in reducing atmospheres to mimic the conditions in a fuel reactor. Additionally, the concept of rapid field reversal could be used in the SID to determine if it is potassium, sodium or a combination of both that leaves the sample. Lastly, experiments with different heating rates could provide valuable information related to the kinetic parameters.

CRediT authorship contribution statement

Viktor Andersson: . **Ivana Staničić:** Writing – review & editing, Methodology, Investigation. **Xiangrui Kong:** . **Henrik Leion:** . **Tobias Mattisson:** Writing – review & editing, Supervision. **Jan B.C. Pettersson:** .

Declaration of Competing Interest

The authors declare that they have no known competing financial interests or personal relationships that could have appeared to influence the work reported in this paper.

Data availability

Data will be made available on request.

Acknowledgments

This work is supported by the Swedish Research Council, project “Biomass combustion chemistry with oxygen carriers” 2016-06023.

Appendix A. Supplementary material

Supplementary data to this article can be found online at https://doi.org/10.1016/j.fuel.2023.130400.

References

[1] Myhre G, Shindell D, Bréon F-M, Collins W, Fuglestvedt J, Huang J, et al. Anthropogenic and Natural Radiative Forcing, Climate change 2013: the physical science basis. In: Stocker TF, Qin D, Plattner G–K, Tignor M, Allen SK, Boschung J, Nauels A, Xia Y, Bex V, Midgley PM, editors. Contribution of Working Group I to the Fifth Assessment Report of the Intergovernmental Panel on Climate Change. Cambridge, United Kingdom and New York, NY, USA: Cambridge University Press; 2013.

[2] United Nations Framework Convention for Climate Change, 2015. https://unfccc.int/process-and-meetings/the-paris-agreement/the-paris-agreement.

[3] Haszeldine RS. Carbon capture and storage: how green can black be? Science 2009; 325(5948):1647. https://doi.org/10.1126/science.1172246.

[4] Johansson F, Kjärstad J, Odenberger M. The importance of CO_2 capture and storage: a geopolitical discussion. Therm Sci 2012;16(3):655–68. https://doi.org/10.2298/tsci120608135j.

[5] Azar C, Johansson DJA, Mattsson N. Meeting global temperature targets—the role of bioenergy with carbon capture and storage. Environ Res Lett 2013;8(3):034004. https://doi.org/10.1088/1748-9326/8/3/034004.

[6] Adánez J, Abad A, Mendiara T, Gayán P, de Diego LF, García-Labiano F. Chemical looping combustion of solid fuels. Prog Energy Combust Sci 2018;65:6–66. https://doi.org/10.1016/j.pecs.2017.07.005.

[7] Lyngfelt A, Leckner B, Mattisson T. A fluidized-bed combustion process with inherent CO_2 separation; application of chemical-looping combustion. Chem Eng Sci 2001;56(10):3101–13. https://doi.org/10.1016/S0009-2509(01)00007-0.

[8] Lyngfelt A. Oxygen carriers for chemical looping combustion - 4000 h of operational experience. Oil Gas Sci Technol - Revue d’IFP Energies nouvelles 2011; 66(2):161–72. https://doi.org/10.2516/ogst/2010038.

[9] Gall D, Pushp M, Larsson A, Davidsson K, Pettersson JBC. Online measurements of alkali metals during start-up and operation of an industrial-scale biomass gasification plant. Energy Fuel 2018;32(1):532–41. https://doi.org/10.1021/acs.energyfuels.7b03135.

[10] Pushp M, Gall D, Davidsson K, Seemann M, Pettersson JBC. Influence of bed material, additives, and operational conditions on alkali metal and tar concentrations in fluidized bed gasification of biomass. Energy Fuel 2018;32(6): 6797–806. https://doi.org/10.1021/acs.energyfuels.8b00159.

[11] Corcoran A, Knutsson P, Lind F, Thunman H. Mechanism for migration and layer growth of biomass ash on ilmenite used for oxygen carrier aided combustion. Energy Fuel 2018;32(8):8845–56. https://doi.org/10.1021/acs.energyfuels.8b01888.

[12] Thunman H, Lind F, Breitholtz C, Berguerand N, Seemann M. Using an oxygen-carrier as bed material for combustion of biomass in a 12-MWth circulating fluidized-bed boiler. Fuel 2013;113:300–9. https://doi.org/10.1016/j.fuel.2013.05.073.

[13] Leckner B. Fluidized bed combustion: mixing and pollutant limitation. Prog Energy Combust Sci 1998;24(1):31–61.

[14] Pallarès D, Johnsson F. Time-resolved modeling of gas mixing in fluidized bed units. Fuel Process Technol 2015;134:73–84. https://doi.org/10.1016/j.fuproc.2015.01.017.

[15] Khan AA, de Jong W, Jansens PJ, Spliethoff H. Biomass combustion in fluidized bed boilers: potential problems and remedies. Fuel Process Technol 2009;90(1): 21–50. https://doi.org/10.1016/j.fuproc.2008.07.012.

[16] Mattisson T, Keller M, Linderholm C, Moldenhauer P, Rydén M, Leion H, et al. Chemical-looping technologies using circulating fluidized bed systems: status of development. Fuel Process Technol 2018;172:1–12. https://doi.org/10.1016/j.fuproc.2017.11.016.

[17] Karami D, Soleimanisalim AH, Sedghkerdar MH, Mahinpey N. Preparation of novel oxygen carriers supported by Ti, Zr-shelled γ-alumina for chemical looping combustion of methane. Ind Eng Chem Res 2020;59(7):3221–8. https://doi.org/10.1021/acs.iecr.9b06832.

[18] Rydén M, Lyngfelt A, Mattisson T. CaMn0.875Ti0.125O3 as oxygen carrier for chemical-looping combustion with oxygen uncoupling (CLOU)—Experiments in a continuously operating fluidized-bed reactor system. Int J Greenhouse Gas Control 2011;5(2):356–66. https://doi.org/10.1016/j.ijggc.2010.08.004.

[19] Linderholm C, Schmitz M, Knutsson P, Lyngfelt A. Chemical-looping combustion in a 100-kW unit using a mixture of ilmenite and manganese ore as oxygen carrier. Fuel 2016;166:533–42. https://doi.org/10.1016/j.fuel.2015.11.015.

[20] Schmitz M, Linderholm CJ. Performance of calcium manganate as oxygen carrier in chemical looping combustion of biochar in a 10kW pilot. Appl Energy 2016;169: 729–37. https://doi.org/10.1016/j.apenergy.2016.02.088.

[21] Adanez J, Abad A, Garcia-Labiano F, Gayan P, de Diego LF. Progress in chemical-looping combustion and reforming technologies. Prog Energy Combust Sci 2012;38 (2):215–82. https://doi.org/10.1016/j.pecs.2011.09.001.

[22] Gyllén A, Knutsson P, Lind F, Thunman H. Magnetic separation of ilmenite used as oxygen carrier during combustion of biomass and the effect of ash layer buildup on its activity and mechanical strength. Fuel 2020;269:117470. https://doi.org/10.1016/j.fuel.2020.117470.

[23] Staničić I, Mattisson T, Backman R, Cao Y, Rydén M. Oxygen carrier aided combustion (OCAC) of two waste fuels - experimental and theoretical study of the interaction between ilmenite and zinc, copper and lead. Biomass Bioenergy 2021; 148:106060. https://doi.org/10.1016/j.biombioe.2021.106060.

[24] M. Zevenhoven, P. Yrjas, M. Hupa, Ash-Forming Matter and Ash-Related Problems, 2010. https://doi.org/10.1002/9783527628148.hoc068.

[25] Corcoran A, Marinkovic J, Lind F, Thunman H, Knutsson P, Seemann M. Ash properties of ilmenite used as bed material for combustion of biomass in a circulating fluidized bed boiler. Energy Fuel 2014;28(12):7672–9. https://doi.org/10.1021/ef501810u.

[26] Mims CA, Pabst JK. Alkali-catalyzed carbon gasification kinetics: Unification of H2O, D2O, and CO2 reactivities. J Catal 1987;107(1):209–20. https://doi.org/10.1016/0021-9517(87)90286-7.

[27] Gall D, Pushp M, Davidsson KO, Pettersson JBC. Online measurements of alkali and heavy tar components in biomass gasification. Energy Fuel 2017;31(8):8152–61. https://doi.org/10.1021/acs.energyfuels.7b00474.

[28] Wang W, Lemaire R, Bensakhria A, Luart D. Review on the catalytic effects of alkali and alkaline earth metals (AAEMs) including sodium, potassium, calcium and magnesium on the pyrolysis of lignocellulosic biomass and on the co-pyrolysis of coal with biomass. J Anal Appl Pyrol 2022;163:105479. https://doi.org/10.1016/j.jaap.2022.105479.

[29] Gogolev I, Linderholm C, Gall D, Schmitz M, Mattisson T, Pettersson JBC, et al. Chemical-looping combustion in a 100 kW unit using a mixture of synthetic and natural oxygen carriers – operational results and fate of biomass fuel alkali. Int J Greenhouse Gas Control 2019;88:371–82. https://doi.org/10.1016/j.ijggc.2019.06.020.

[30] Eriksson J-E, Zevenhoven M, Yrjas P, Brink A, Hupa L. Corrosion of heat transfer materials by potassium-contaminated ilmenite bed particles in chemical-looping combustion of biomass. Energies 2022;15(8):2740. https://doi.org/10.3390/en15082740.

[31] Chanpirak A, Hashemi H, Frandsen FJ, Wu H, Glarborg P, Marshall P. The chemical coupling between moist CO oxidation and gas-phase potassium sulfation. Fuel 2023;336:127127. https://doi.org/10.1016/j.fuel.2022.127127.

[32] Gogolev I, Soleimanisalim AH, Linderholm C, Lyngfelt A. Commissioning, performance benchmarking, and investigation of alkali emissions in a 10 kWth solid fuel chemical looping combustion pilot. Fuel 2021;287:119530. https://doi.org/10.1016/j.fuel.2020.119530.
[33] Öhman M, Nordin A, Skrifvars B-J, Backman R, Hupa M. Bed agglomeration characteristics during fluidized bed combustion of biomass fuels. Energy Fuel 2000;14(1):169–78. https://doi.org/10.1021/ef990107b.
[34] Staničić I, Andersson V, Hanning M, Mattisson T, Backman R, Leion H. Combined manganese oxides as oxygen carriers for biomass combustion — ash interactions. Chem Eng Res Des 2019;149:104–20. https://doi.org/10.1016/j.cherd.2019.07.004.
[35] Link S, Yrjas P, Lindberg D, Trikkel A. Characterization of ash melting of reed and wheat straw blend. ACS Omega 2022;7(2):2137–46. https://doi.org/10.1021/acsomega.1c05087.
[36] Hildor F, Zevenhoven M, Brink A, Hupa L, Leion H. Understanding the interaction of potassium salts with an ilmenite oxygen carrier under dry and wet conditions. ACS Omega 2020;5(36):22966–77. https://doi.org/10.1021/acsomega.0c02538.
[37] Lu DY, Tan Y, Duchesne MA, McCalden D. Potassium capture by ilmenite ore as the bed material during fluidized bed conversion. Fuel 2023;335:127008. https://doi.org/10.1016/j.fuel.2022.127008.
[38] Staničić I, Hanning M, Deniz R, Mattisson T, Backman R, Leion H. Interaction of oxygen carriers with common biomass ash components. Fuel Process Technol 2020;200:106313. https://doi.org/10.1016/j.fuproc.2019.106313.
[39] Andersson V, Ge Y, Kong X, Pettersson JBC. A novel method for on-line characterization of alkali release and thermal stability of materials used in thermochemical conversion processes. Energies 2022;15(12):4365. https://doi.org/10.3390/en15124365.
[40] P. Moldenhauer, A. Gyllén, H. Thunman, F. Lind, A Scale-Up Project for Operating a 115 MWth Biomass-Fired CFB boiler with Oxygen Carriers as Bed Material, 2018.
[41] Davidsson K, Engvall K, Hagström M, Korsgren J, Lönn B, Pettersson J. A surface ionization instrument for on-line measurements of alkali metal components in combustion: instrument description and applications. Energy Fuels 2002;16. https://doi.org/10.1021/ef020020h.
[42] Paatero P, Tapper U. Positive matrix factorization: a non-negative factor model with optimal utilization of error estimates of data values. Environmetrics 1994;5(2):111–26. https://doi.org/10.1002/env.3170050203.
[43] Kong X, Salvador CM, Carlsson S, Pathak R, Davidsson K, Le Breton M, et al. Molecular characterization and optical properties of primary emissions from a residential wood burning boiler. Sci Total Environ 2020;754:142143. https://doi.org/10.1016/j.scitotenv.2020.142143.
[44] G. Norris R. Duvall S. Brown S. Bai EPA positive matrix factorization (PMF) 5.0 fundamentals and user guide 2014 Washington, DC.
[45] X. Kong, I. Staničić, V. Andersson, T. Mattisson, J.B.C. Petterson, Phase Recognition in SEM-EDX Chemical Maps using Positive Matrix Factorization MethodsX co-submission; 2023.
[46] J.F. Moulder W.F. Stickle P.E. Sobol K.d. Bomben, Handbook of X-ray Photoelectron Spectroscopy - A Reference Book of Standard Spectra for Identification and Interpretation of XPS Data, Perkin-Elmer Corporation - Physical Electronics Division, 6509 Flying Cloud Drive Eden Prairie 1992 United Stales of America Minnesota 55344.
[47] Kondratev VN. Chemical Kinetics of Gas Reactions. London, England: Pergamon Press; 1964.
[48] Faust R, Valizadeh A, Qiu R, Tormachen A, Maric J, Vilches TB, et al. Role of surface morphology on bed material activation during indirect gasification of wood. Fuel 2023;333:126387. https://doi.org/10.1016/j.fuel.2022.126387.
[49] Staničić I, Brorsson J, Hellman A, Mattisson T, Backman R. Thermodynamic analysis on the fate of ash elements in chemical looping combustion of solid fuels—iron-based oxygen carriers. Energy Fuel 2022;36(17):9648–59. https://doi.org/10.1021/acs.energyfuels.2c01578.
[50] Gall D, Nejman C, Allguren T, Andersson K, Pettersson JBC. A new technique for real-time measurements of potassium and sodium aerosols based on field-reversal surface ionization. Meas Sci Technol 2021;32(7):075802. https://doi.org/10.1088/1361-6501/abe130.
[51] Ströhle J, Orth M, Epple B. Design and operation of a 1MWth chemical looping plant. Appl Energy 2014;113:1490–5. https://doi.org/10.1016/j.apenergy.2013.09.008.